



ELSEVIER

Available online at www.sciencedirect.com



Comput. Methods Appl. Mech. Engrg. 192 (2003) 2481–2499

**Computer methods
in applied
mechanics and
engineering**

www.elsevier.com/locate/cma

A boundary element technique for incremental, non-linear elasticity Part II: Bifurcation and shear bands

M. Brun^a, D. Bigoni^{a,*}, D. Capuani^b

^a *Dipartimento di Ingegneria Meccanica e Strutturale, Università di Trento, Via Mesiano 77,
I-38050 Povo, Trento, Italy*

^b *Dipartimento di Ingegneria, Università di Ferrara, Via Saragat 1, 44100 Ferrara, Italy*

Received 19 November 2002; accepted 11 February 2003

Abstract

Incremental elastic deformations superimposed upon a given homogeneous strain are analyzed employing the boundary element technique developed in Part I of this study. As a consequence of the fact that the formulation fully embodies non-linear effects, the proposed approach yields bifurcation loads and associated deformation modes. In particular, bifurcations of elastic structures are investigated, including cracked bodies and multilayers. As special cases of instability not involving length scales, surface bifurcations and shear bands are analyzed and they are both found to occur within the elliptic range, as induced by perturbations.

© 2003 Elsevier Science B.V. All rights reserved.

1. Introduction

In Part I of this study a boundary element formulation has been given, based on early work by Bigoni and Capuani [11]. In particular, two-dimensional, incremental non-linear deformations are considered from a given, homogeneously stressed configuration. Since the formulation fully embodies large strain effects, it allows the determination of bifurcation loads and modes. A systematic investigation of these is the focus of this second part, with emphasis on special situations including multilayered and cracked bodies. The results may find broad applications and, in particular, numerical simulations are presented which may be useful in the design of rubber bearings employed in earthquake-resistant design of buildings.

Two peculiar kinds of bifurcations are given special attention: corresponding to the so-called ‘surface instability’ and ‘shear banding’, the latter associated to the condition of loss of ellipticity. Both bifurcations represent ill-posedness of the incremental problem and are characterized by the fact that the bifurcation mode embodies an arbitrarily-short wave length. This gives rise to well-known difficulties in finite element

* Corresponding author. Tel.: +39-0461-882507; fax: +39-0461-882599.

E-mail addresses: michele.brun@ing.unitn.it (M. Brun), bigoni@ing.unitn.it (D. Bigoni), cpd@dns.unife.it (D. Capuani).

URL: <http://www.ing.unitn.it/~bigoni/>.

simulations. However, while there is an immense literature on numerical investigation of shear bands, numerical treatments of surface instability are scarce [4,27,54]. This is rather surprising, since both instabilities are *local* and involve similar problems.

Many routes have been proposed to numerically regularize a problem *beyond* the elliptic range. In particular, a class of approaches consists in modifying the constitutive models to include an intrinsic characteristic length. Non-local constitutive models [5,33,44], Cosserat continua [16,35], visco-plastic models [34,38], and higher-order gradient models [17,23,24,36,50,52,56] fall within this class. In another class of approaches, numerical regularization is pursued by introducing *ad hoc* special interpolating functions at element level [6,32,37,43], or by embedding strong discontinuities [2,3,15,39,49]. All the above-mentioned approaches are based on finite element techniques, while the only analysis with the boundary element method is quite recent [9]. This is again surprising, since BEM are known to be an efficient tool in problems involving concentration of deformations, such as for instance in fracture mechanics [1,18].

It is clear from the above discussion that analysis of strain localization in solids has been a topic for years in the numerical community. Nevertheless, the problem is far from being solved, so that while on one hand commercial codes do not still incorporate features for automatic shear band analysis, on the other hand many fundamental aspects—such as for instance propagation conditions at the shear band tip—still remain almost completely unexplored.

A common denominator of the former class of the above-mentioned strategies is that they represent a restoration of ellipticity of governing equations [7,8]. In contrast to this general situation, two different approaches were recently initiated by Petryk and Thermann [41,42] and Bigoni and Capuani [11], characterized by the fact that, for completely different reasons, the restoration of ellipticity is avoided. In the former approach, devoted to incrementally non-linear materials, path-stability criterion [40] is sufficient to determine the volume fraction and thus the overall behaviour of material elements in a post-critical range. In the latter approach, strain localization is analyzed in the *proximity* of the ellipticity boundary, as induced by a perturbation, still inside the region of ellipticity. As a result of perturbation, introducing in a sense a length scale, localized deformation patterns emerge. For instance, Bigoni and Capuani [11] have shown that localized deformations may be observed in a Mooney–Rivlin material, which is known to remain within the elliptic range. A goal of the present study is to continue the investigation by extending the approach to boundary value problems and employing the boundary element technique developed in Part I of this article. Obviously, special numerical strategies are completely avoided since the analysis is performed within the elliptic range. Results demonstrate that the boundary element technique is particularly suitable to the analysis of surface instability and shear band formation.

2. Bifurcation of elastic structures

A Fortran 95 code with dynamic allocation of memory has been implemented to develop applications of the boundary element technique presented in Part I. Integrals are computed numerically, using Gaussian quadrature formulae with 12 integration points for Green's functions (see Part I) and 18 points for integrals in the discretized boundary integral equation (see Part I), unless otherwise specified. Several examples—considering small strains superimposed upon homogeneous, arbitrarily large deformations—are provided below demonstrating the capabilities of the method.

2.1. Elastic block

An elastic block is considered, in a square (the edge length of the block has been taken equal to $2b$), stressed current configuration, for a Mooney–Rivlin material. A uniaxial state of stress is prescribed in terms of the non-dimensional parameter k defined as

$$k = \frac{\sigma}{2\mu} = \frac{\sigma_1 - \sigma_2}{2\mu} = \frac{\lambda_1^2 - \lambda_2^2}{\lambda_1^2 + \lambda_2^2}, \tag{1}$$

where σ_1 (assumed zero in the following) and σ_2 are the principal Cauchy stresses—so that σ is the current deviatoric, in-plane stress— μ is the incremental modulus for shear parallel to the principal Eulerian axes and λ_1, λ_2 are the in-plane stretches. Bifurcations from this state were analyzed by Biot [14], Hill and Hutchinson [25] and Young [57], considering a smooth bilateral constraint at the two edges normal to the direction of the uniaxial stress. For Mooney–Rivlin material, bifurcations are only possible in compression, where it turns out that the first bifurcation occurs at $k \approx 0.522$, corresponding to an antisymmetric mode with a ratio $\lambda/(2b) = 2$ between wave length λ and edge length. Above this bifurcation value, an infinite set of critical values of k follows, corresponding to antisymmetric bifurcations. The accumulation point of these values defines the surface instability, occurring at $k \approx 0.839$, solution, with reversed sign, of the equation (see [45], their Eq. (3.16) with $\xi = 1$)

$$\frac{k}{2} \left(1 - \sqrt{\frac{1-k}{1+k}} \right) - 1 = 0 \tag{2}$$

and corresponding to the limit $\lambda/(2b) = 0$. For values of k greater than the surface instability threshold, an infinite set of symmetric bifurcation becomes possible, bounded by $k \approx 0.926$ for $\lambda/2b = 2/3$,¹ which is the highest value of k corresponding to a bifurcation obtained as a linear combination of wave modes

$$v_l = a_l e^{i\kappa(\sqrt{\gamma_j}x_1+x_2)}, \quad \dot{p} = c e^{i\kappa(\sqrt{\gamma_j}x_1+x_2)}, \tag{3}$$

where v_l is the velocity, \dot{p} is the in-plane pressure rate, $i = \sqrt{-1}$, a_l and c are complex amplitudes, γ_j ($j = 1, 2$) are the roots of the characteristic equation (see Part I) and κ is the wave number of the bifurcation mode. Therefore, the surface instability ‘separates’ the two infinite sets of antisymmetric and symmetric bifurcation modes. Some critical values of k and the corresponding modal wavelength $\lambda/2b$ are reported in the second and third column of Table 1.

For the above described geometry, bifurcation points can be numerically traced by analyzing the eigenvalue problem associated to the boundary element discretization. In our case, two uniform meshes of 72 and 144 elements (denoted as ‘coarse’ and ‘fine’ in the following) have been chosen. The upper and lower edges of the block have been constrained with smooth rigid boundaries (the lower central node has been fixed to eliminate possibility of rigid body translations) and the determinant of the solving system has been analyzed at different values of pre-stress k . The results are reported in the fourth and fifth column of Table 1. We note that while the initial and final critical values k are computed with an excellent accuracy, values getting close to the accumulation point can be hardly detected numerically.

However, bifurcations can also be analyzed using a perturbation technique. In particular, we may start from the above geometry, with the velocities prescribed to be zero along the lower edge. In this situation we may assign symmetric or antisymmetric perturbations in terms of dead loading along the free edges. It may be anticipated that the symmetry of the perturbation will trigger a correspondingly symmetric bifurcation mode. Let us analyze the two kinds of perturbations in detail.

2.1.1. Antisymmetric perturbation and Euler-type instability

As is shown in Fig. 1, the lateral faces of the block, initially free, are subsequently subject to perturbations, in terms of antisymmetric, normal incremental dead-load. Referring to a Mooney–Rivlin material

¹ There is a systematic misprint in the discussion of the example in Section 6.1 of [11]. All the values $\lambda/2b$ should be read there as $2b/\lambda$.

Table 1
Bifurcation pre-stress k and relative mode for a square elastic, Mooney–Rivlin block

Analytical			Numerical	
Mode	$\lambda/2b$	k	k for fine mesh	k for coarse mesh
Anti	2	0.522	0.522	0.523
Anti	1	0.732	0.733	0.735
Anti	2/3	0.796	0.797	0.802
Anti	1/2	0.821	0.824	0.832
Anti	2/5	0.832	0.836	–
Anti	1/3	0.836	–	–
Anti	2/7	0.838	–	–
Anti	–	–	–	–
–	0	0.839	–	–
Sym	–	–	–	–
Sym	2/7	0.841	–	–
Sym	1/3	0.843	0.849	–
Sym	2/5	0.849	0.854	0.869
Sym	1/2	0.866	0.867	0.880
Sym	2/3	0.926	0.930	0.939

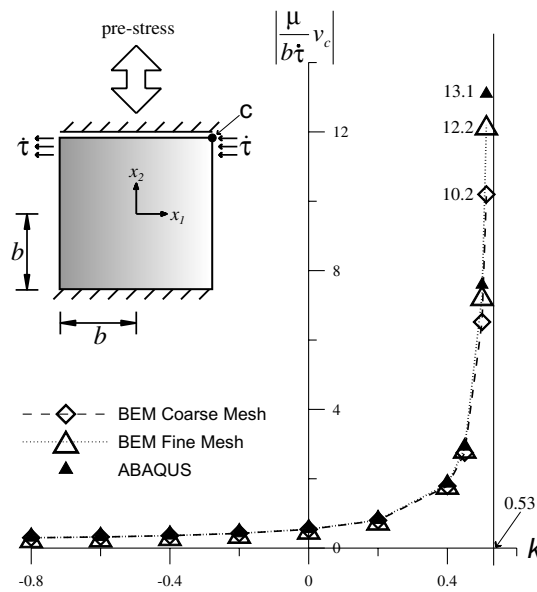


Fig. 1. Non-dimensionalized velocity of the corner point c versus pre-stress k .

and to the coarse and fine meshes already employed, the portion of the edges subject to incremental load has been taken equal to 1/9 of the total edge length. The results of numerical investigation are reported in Figs. 1 and 2. The velocity v_c at the upper point of the right edge (non-dimensionalized as $\mu v_c / (b\dot{\tau})$, where b is the half-length of the edge and $\dot{\tau}$ is the applied nominal traction rate) is plotted versus the pre-stress k in Fig. 1, where the computed values are marked for $k = \{-0.8, -0.6, -0.4, -0.2, 0, 0.2, 0.4, 0.45, 0.5, 0.5125\}$. The profiles of velocity components (multiplied by $\mu / (b\dot{\tau})$) along the vertical edge are shown in Fig. 2 for different values of k . Comparisons are included with results obtained using ABAQUS-Standard (Ver. 6-2-Hibbitt, Karlsson & Sorensen Inc.), with plane-strain, 4-nodes bilinear, hybrid elements (CPE4H).

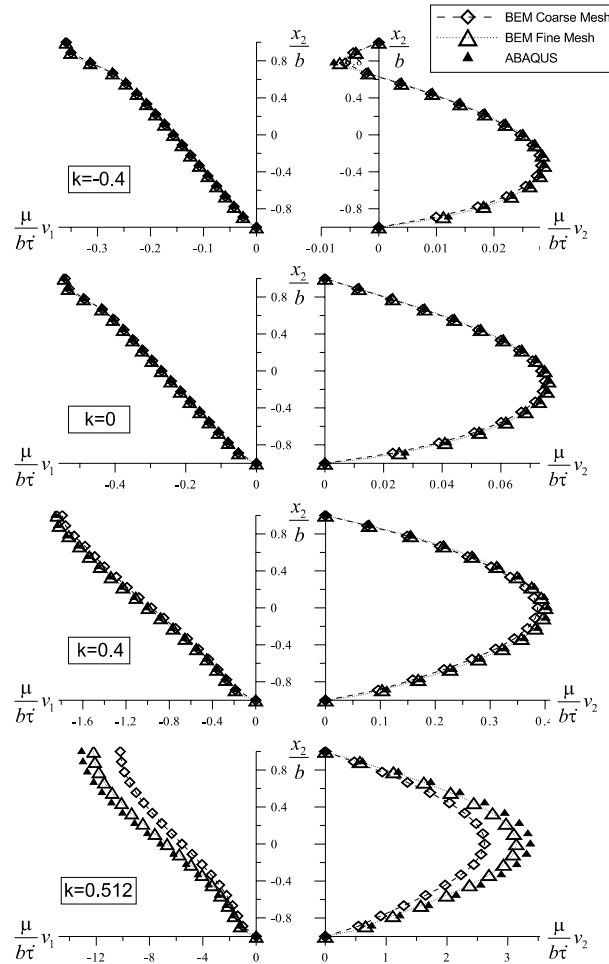


Fig. 2. Velocity profiles along the vertical edge, for the geometry specified in the detail of Fig. 1.

An analysis of Fig. 1 reveals that stiffness in the incremental response varies significantly as a function of the pre-stress. In particular, traction (corresponding to negative values of k) increases stiffness, whereas compression (corresponding to positive values of k) induces stiffness degradation. The latter becomes dramatic when a critical value of k is reached. This is found to range between 0.5336 and 0.5344 (at which value the stiffness becomes negative) for the coarse mesh, between 0.5289 and 0.5297 for the fine mesh and between 0.5281 and 0.5289 for Finite Element analysis. Though relative to a slightly different boundary condition at the lower edge, this result agrees with the bifurcation analysis (Table 1).

Profiles of velocities components along the edge are shown in Fig. 2 for $k = \{-0.4, 0, 0.4, 0.5125\}$. Results of ABAQUS are in excellent agreement with those obtained with our boundary element technique up to $k = 0.4$; in the case when $k = 0.5125$ the qualitative behaviour is still well captured.

Incremental displacement fields are reported in Fig. 3, where we note that the qualitative deformations are similar, but the quantitative incremental displacements tend to blow up, when the bifurcation point is approached. We can also note that the bifurcation mode is similar to a Euler-type deformation, corresponding to a beam restrained to rotate at the edges.

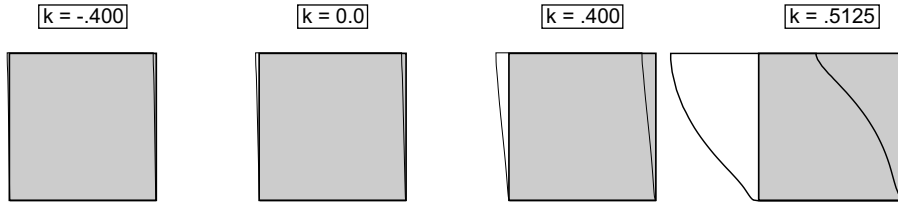


Fig. 3. Qualitative deformations at different values of pre-stress k , for antisymmetric perturbation. The geometry is specified in the detail of Fig. 1.

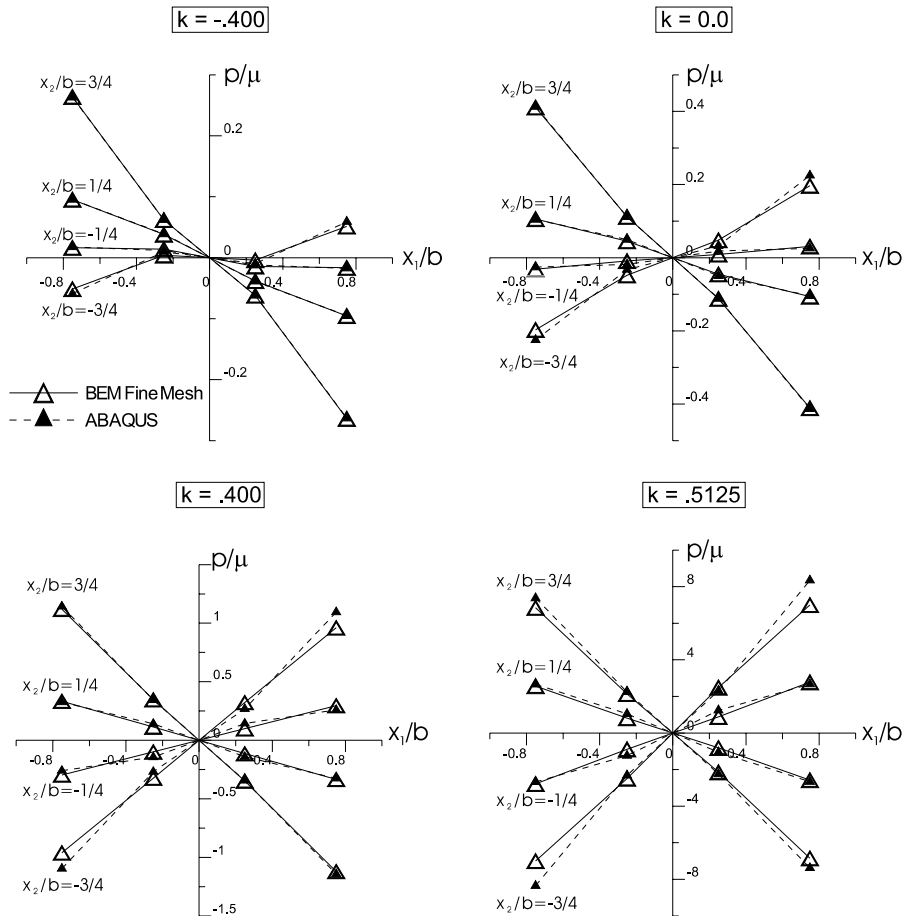


Fig. 4. Values of internal in-plane pressure rate at different values of pre-stress k , for the geometry specified in the detail of Fig. 1. Comparison with results obtained with ABAQUS is also reported.

Internal fields can be obtained using boundary integral equations for the velocity and for the in-plane pressure rate (see Part I). In particular, results obtained employing a discretized version of the boundary integral equation for pressure rate (see Part I) are reported in Fig. 4, showing the in-plane pressure rate field (normalized through division by μ) at inner points, with coordinates $x_1/b = \{-0.75, -0.25, 0, 0.25, 0.75\}$

and $x_2/b = \{-0.75, -0.25, 0, 0.25, 0.75\}$. The points having the same co-ordinate x_2 are connected by lines. Four levels of pre-stress $k = \{-0.4, 0, 0.4, 0.5125\}$ have been considered and the results are compared to those calculated using ABAQUS with constant pressure elements. The fair agreement of the results represents the first numerical validation of the boundary equation for in-plane pressure rate obtained by Bigoni and Capuani [11].

2.1.2. Symmetric perturbation and surface instability

Let us consider now the symmetric perturbation sketched in Fig. 5, considering the same setting of the previous, antisymmetric situation. The velocity of the middle point of the edge versus the pre-stress k is reported in Fig. 5. It is clear from the figure that the finer is the mesh, the closest is the zero-stiffness asymptote to the surface instability, $k = 0.839$. The wavy deformation mode associated to a localized surface bifurcation is made visible in Fig. 6, where incremental displacement fields are reported. Differently from the antisymmetric situation (Fig. 1) we may note here that the deformation mode changes qualitatively, in the sense that waviness increases when the bifurcation is approached. In particular, three wavelengths are visible in Fig. 6 when the surface instability is approached. For a finer mesh of 36×144 elements the surface instability is approached at $k = 0.842$ and the qualitative deformation shown in Fig. 7 displays nine wavelengths.

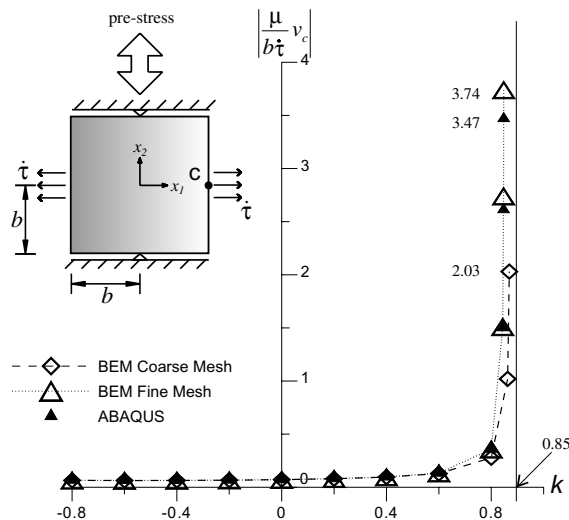


Fig. 5. Non-dimensionalized velocity of the middle point c versus pre-stress k .

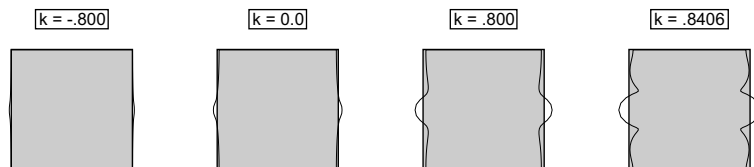


Fig. 6. Qualitative deformations at different values of pre-stress k , for symmetric perturbation. The geometry is specified in the detail of Fig. 5.

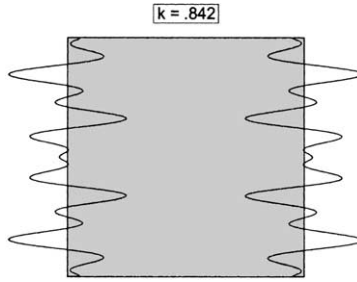


Fig. 7. Qualitative deformation near to surface instability.

2.2. Layered elastic material

The layered elastic structure sketched in the detail of Fig. 8 is now considered. The structure is made up of three layers, with a ‘material 1’ common to the outer layers and a different ‘material 2’ forming the core. Three cases are considered for the ratios of incremental shear moduli $(\mu_*/\mu)_1$, $(\mu_*/\mu)_2$ and μ_1/μ_2 of the two materials and relevant values are reported in Table 2. All layers are specified to undergo the same homogeneous, plane strain deformation with the principal directions of deformation aligned normal and parallel to the layers, as considered in [12,13]. Therefore, a uniaxial state of traction or compression prevails in the laminate. Starting from this pre-stressed state, an incremental, antisymmetric loading $\hat{\tau}$ is prescribed (orthogonal to the external vertical edges of the structure) applied on a loading zone equal to $2b/15$, with b denoting the half-length of the laminate edge (see the detail in Fig. 8). Calculations have been performed with a uniform mesh of 80 elements for each layer and results are reported in Fig. 8, where the velocity (normalized through multiplication by $\mu_1/(b\hat{\tau})$) is plotted versus the pre-stress k . It should be noted that the values of k are independent of the material, since they depend only on the in-plane stretch (1), identical in

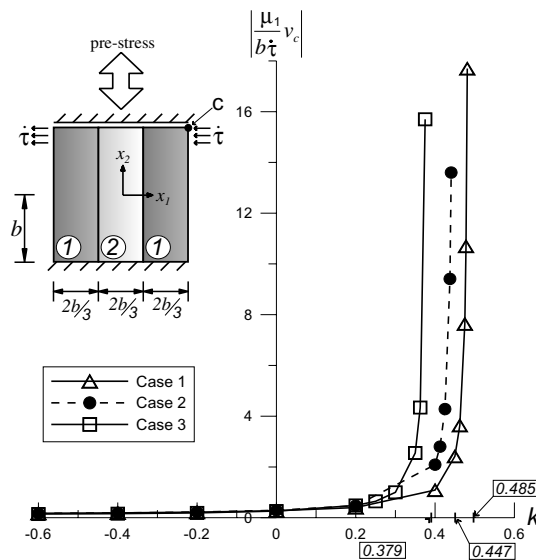


Fig. 8. Non-dimensionalized velocity of the corner point c versus pre-stress k for an elastic laminate.

Table 2
Bifurcation stress k for the layered elastic structure

Case	Shear modulus ratios			Bifurcation stress k	
	$(\mu_*/\mu)_1$	$(\mu_*/\mu)_2$	μ_1/μ_2	Analytical ^a	Numerical
1	1.0	0.5	0.5	0.4722	0.4852–0.4859
2	2/3	1.0	1.5	0.4386	0.4469–0.4477
3	0.5	1.0	2.0	0.3714	0.3789–0.3797

^aThe analytical results refer to slightly different boundary conditions than those employed for the numerical analysis.

all layers. The bifurcation values of k , obtained by the boundary element method, are also reported in Table 2, where they are compared with the analytical values given by Bigoni and Gei [12], under the slightly different boundary condition of smooth rigid contact in the lower edge.

2.3. Cracked elastic blocks

A pre-stressed, rectangular ($3b \times 2b$) elastic block is considered, containing cracks parallel to the free edges. Three cracked configurations are chosen as sketched in the particular of Fig. 9 and the response to a symmetric perturbation is analyzed at different levels of pre-stress k . The perturbation consists of a uniform nominal loading rate along the entire lateral edges which are free until the instant of the perturbation, inducing Mode I near-tip fields. For this situation, no analytical solutions are available, with the exception of the asymptotic near-tip representation obtained in [45]. The incremental displacements at a characteristic

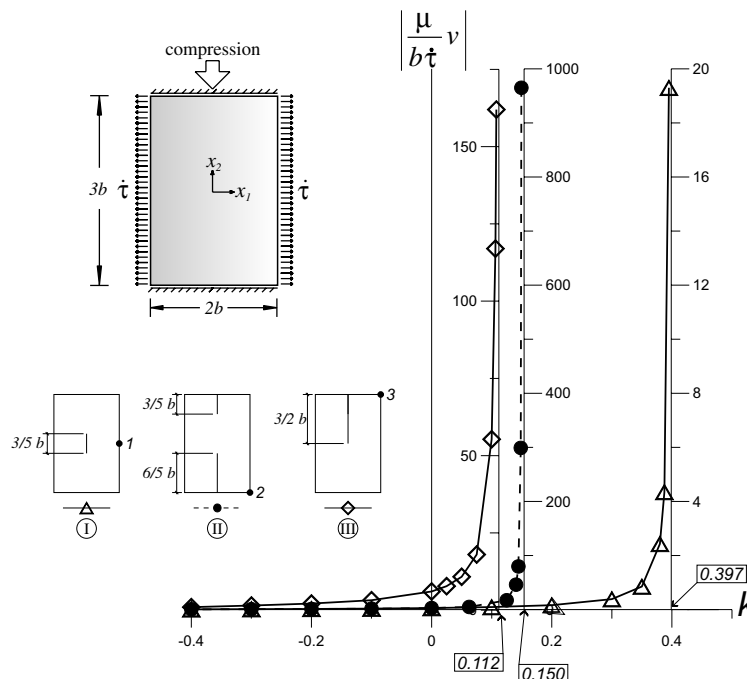


Fig. 9. Non-dimensionalized velocity (versus pre-stress k) at a characteristic point of each cracked configuration (points 1, 2, 3 for configurations I, II, III, respectively).

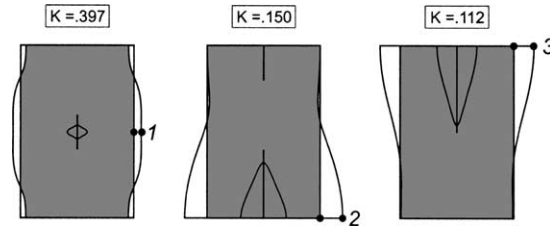


Fig. 10. Deformed configurations in proximity of bifurcation of the cracked elastic blocks.

point of each cracked geometry are plotted in Fig. 9, where the asymptotes correspond to the first bifurcation value $k = \{0.112, 0.150, 0.397\}$. The deformed configurations of the cracked bodies, for values of k close to bifurcation are illustrated in Fig. 10. In the analysis the unilateral contact of the crack faces has been taken into account. A peculiar effect is visible in the geometry II of Fig. 10, where the upper crack remains closed, due to the high value of k . Analyses not reported here have shown that the same crack opens for values of $k \leq 0.0625$.

2.4. An application to rubber bearings

Steel-laminated elastomeric bearings are structural elements widely used in bridges and in buildings as seismic isolators [31]. These are made up of alternate steel and rubber laminates, bonded together. The presence of steel layers increases the vertical stiffness, while the rubber layers permit large shear deformations. The design of bearings is strongly conditioned by stability considerations, so that bridge specifications usually limit their height-to-width ratio. For the evaluation of stability of rubber bearings a number of models at different levels of accuracy has been proposed [19,28,30,31,51,53].

As a practical application of the proposed boundary element formulation, we develop here a simple model to evaluate the incremental, horizontal stiffness of elastomeric bearings as a function of the vertical applied load. In particular, we assume a plane strain situation in which the vertical load produces a homogeneous deformation of the rubber layers corresponding to uniaxial compressive stress. Although this assumption is generally violated due to the bonding between steel and rubber, we find reasonable predictions. As is shown in Fig. 11, we consider a rubber bearing—similar to that employed by [29] (their Fig. 2), but in plane strain—made up of three steel layers (thickness 3 mm) and two rubber layers (thickness 8 mm), with a total height h of 25 mm and we investigate two aspect ratios $h/b = 1/16$ and $h/b = 1/8$. The rubber layers are Mooney–Rivlin materials, defined by the strain energy function

$$W(I_1, I_2) = \frac{\mu_1}{2} (I_1 - 3) - \frac{\mu_2}{4} (I_1^2 - I_2 - 6), \tag{4}$$

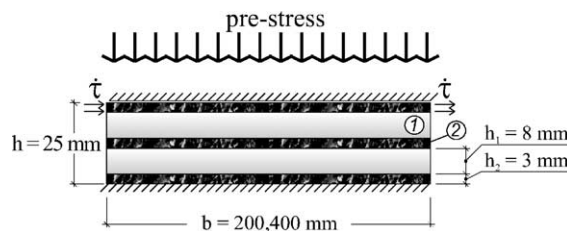


Fig. 11. Geometry of the analyzed rubber bearings.

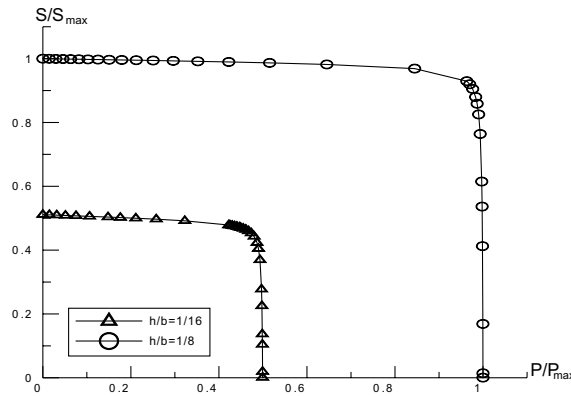


Fig. 12. Influence of the vertical load on the horizontal stiffness.

with $\mu_1 = 0.599$ MPa and $\mu_2 = -0.108$ MPa. Horizontal stiffness has been obtained calculating the horizontal displacement induced by a horizontal antisymmetric loading applied over the thickness of the upper (steel) layer (Fig. 11). Results are reported in Fig. 12, where the horizontal stiffness (normalized with respect to the maximum stiffness of the wider bearing $S_{\max} = 5.403$ MPa) versus applied vertical load (normalized with respect to the maximum vertical load of the wider bearing $P_{\max} = 2.025 \times 10^6$ N/m) are reported.

3. Shear bands within the elliptic range

Let us consider an incompressible body characterized by the constitutive equation introduced in Part I and relating the material derivative of nominal stress to the velocity gradient as

$$\dot{t}_{ij} = \mathbb{K}_{ijkl}v_{l,k} + \dot{p}\delta_{ij}, \quad v_{i,i} = 0, \tag{5}$$

where \dot{p} is the in-plane pressure rate and \mathbb{K}_{ijkl} is the constitutive fourth-order tensor having the major symmetry. It is well-known that shear bands represent an extreme form of material instability, corresponding to failure of ellipticity

$$n_i \mathbb{K}_{ijhk} n_h g_k = 0, \quad \text{subject to } n_k g_k = 0, \tag{6}$$

for at least one unit vector n_k and non-null orthogonal vector g_k . Condition (6) can be shown to yield the classical regime classification (Appendix A).

In a continuous loading program, loss of ellipticity can occur *after* various bifurcation thresholds are attained. For instance, in the examples presented in the previous section shear bands may only occur well after the detected bifurcation points. As a consequence, shear banding must be analyzed when the structure is in a post-critical range (a circumstance usually overlooked in the literature). This is not an easy task, since in that case the current state is inhomogeneous. However, there is a special case where shear bands may occur as the first possible bifurcation. This is the so-called ‘van Hove condition’, in which the solid is subject to prescribed displacements over the entire boundary and the current state (deformation and stress) is homogeneous [55]. More in detail, the incremental solution is unique—unless an arbitrary uniform pressure—until the strong ellipticity condition holds

$$g_j n_i \mathbb{K}_{ijhk} n_h g_k > 0, \quad \text{subject to } n_k g_k = 0, \tag{7}$$

for all pair of orthogonal vectors n_k and g_k . However, it is clear from the definitions (6) and (7) that
 strong ellipticity \Rightarrow ellipticity

and that for \mathbb{K} possessing the major symmetry,² the first failure of strong ellipticity in a continuous loading program corresponds to failure of ellipticity and shear band formation. Therefore, we consider van Hove conditions, assuming the geometric setting shown in Fig. 13, where a square elastic block is considered, homogeneously deformed in a state of uniaxial tension or compression. Displacements are prescribed on the entire boundary, so that the solution is known unless an arbitrary value of homogeneous pressure. We assume $\mu_*/\mu = 0.25$, corresponding to the elliptic complex regime, and perturb this configuration prescribing the triangular distributions of velocity sketched in Fig. 13. The perturbation is characterized by the ratio of the maximum assigned velocity to the length of the application zone. This ratio has been assumed equal to 9/20 and 9/40 on the left and right edge, respectively, of the block in Fig. 13. Results of computations—in terms of level sets of the velocity modulus—are reported in Figs. 14 and 16, the former relative to $c/b = 1/2$, the latter to $c/b = 4/9$.

Level sets of the modulus of the in-plane deviatoric stress increment (normalized through division by μ)

$$\frac{|\dot{\sigma}|}{\sqrt{2}\mu} = \frac{|\dot{\sigma}_1 - \dot{\sigma}_2|}{\sqrt{2}\mu} \quad (8)$$

are also reported in Figs. 15 and 17 and referred to as ‘von Mises stress increment’ in the following. It may be interesting to note that the in-plane deviatoric stress increment coincides for the J_2 -deformation theory of plasticity (see Part I) with the three-dimensional deviatoric stress increment

$$\text{dev } \dot{\sigma} = \dot{\sigma} - \frac{\text{tr } \dot{\sigma}}{3} \mathbf{I}, \quad (9)$$

since the out-of-plane stress increment is equal to $(\dot{\sigma}_1 + \dot{\sigma}_2)/2$ for the J_2 -deformation theory.

A 144-element uniform mesh has been employed to discretize the boundary and a 324-point uniform grid has been used to evaluate the interior velocity field. The Gauss points for the numerical integrations have been increased to 48.

Three different situations are reported in the figures, corresponding to three different values of pre-stress $k = \{-0.859, 0, 0.859\}$. The values ± 0.859 are close to the boundary of loss of ellipticity, occurring at $k = \pm 0.866025$. When the elliptic boundary is attained, shear bands become possible, inclined at an angle η solution of the equation [25]

$$\tan^2 \eta = \frac{1 + 2\sqrt{\mu_*/\mu(1 - \mu_*/\mu)}}{1 - 2\mu_*/\mu}, \quad (10)$$

which, in the special case of $\mu_*/\mu = 0.25$, gives a band inclination $\eta = 27.367^\circ$, with respect to the direction of the maximum in-plane stress component.

It can be seen from Figs. 14 and 16 that when the elliptic boundary is approached, the velocity tends to localize along well-defined shear band patterns. They highlight the inclinations of the discontinuity bands formally possible only at the elliptic boundary.

The fact that strain localization can be observed within the elliptic range employing a perturbation approach agrees with findings by Bigoni and Capuani [11]. On the other hand, it may provide an explanation of the fact that shear banding is a preferred instability when compared to other diffuse bifurcations, possible at loss of ellipticity under van Hove conditions [48].

² The more general case in which the constitutive operator is not symmetric is treated in detail by Bigoni [10].

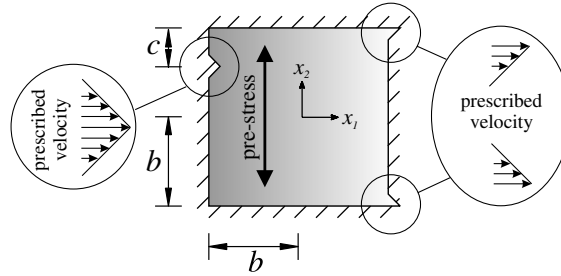


Fig. 13. Loading geometry in van Hove conditions.

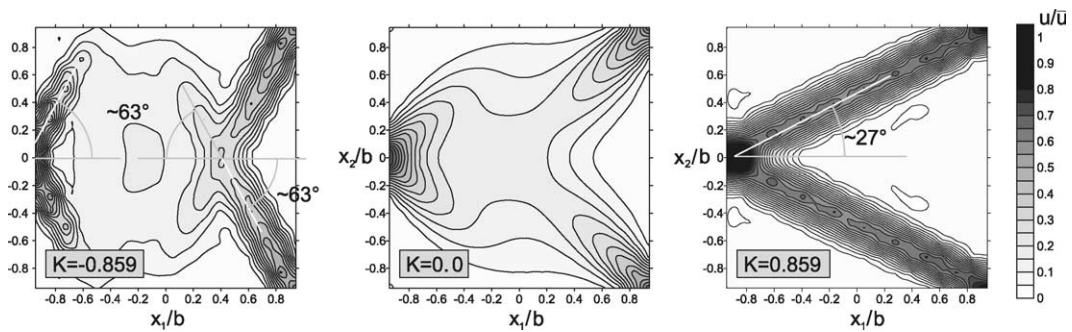


Fig. 14. Van Hove conditions: level sets of velocity modulus at different values of pre-stress k ($c/b = 1/2$ in Fig. 13).

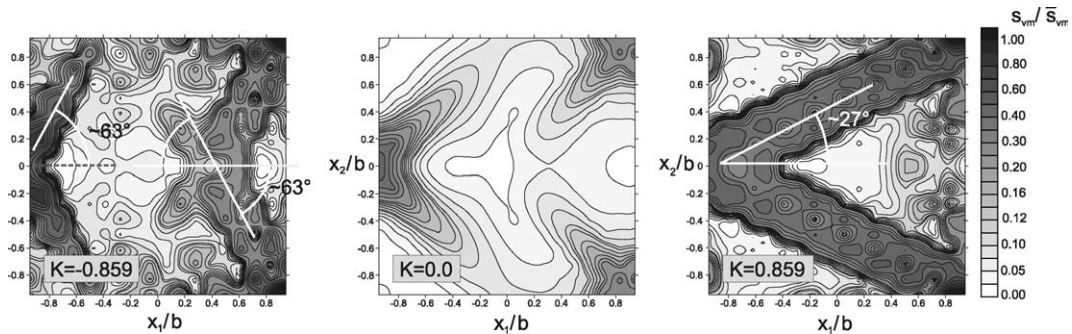


Fig. 15. Van Hove conditions: level sets of von Mises stress increment at different values of pre-stress k ($c/b = 1/2$ in Fig. 13).

The van Hove conditions are very peculiar and provide the maximum possible ‘confinement’ to a material sample. Referred to the case of compressible materials, Ryzhak has shown [46,47] that the van Hove theorem can be extended to a less restrictive condition, that will be called ‘weak van Hove’ in the following. In particular, the material must be homogeneous and orthotropic, with orthotropy axes parallel and orthogonal to the given loading direction. Instead of the usual prescription on displacement, now two parallel edges can be in smooth (bilateral) contact with a rigid constraint (the lubricated ends employed by Biot [14] to explain the so-called ‘internal instabilities’). This is the situation sketched in Fig. 18 which we employ as a current configuration to be perturbed with two assigned, triangular velocity distributions. As in

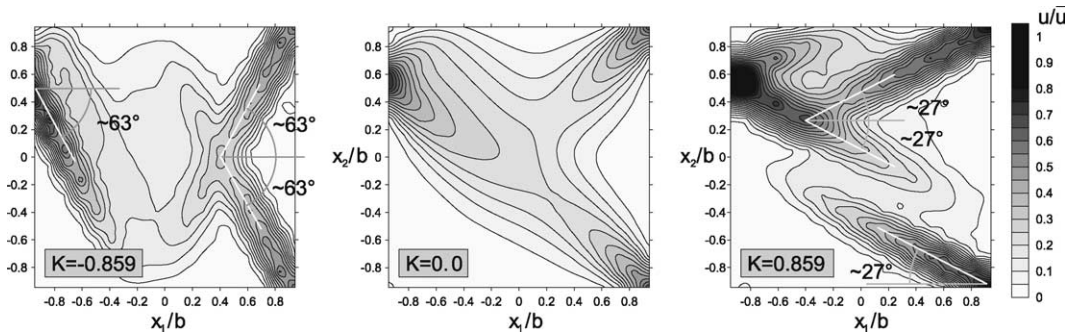


Fig. 16. Van Hove conditions: level sets of velocity modulus at different values of pre-stress k ($c/b = 4/9$ in Fig. 13).

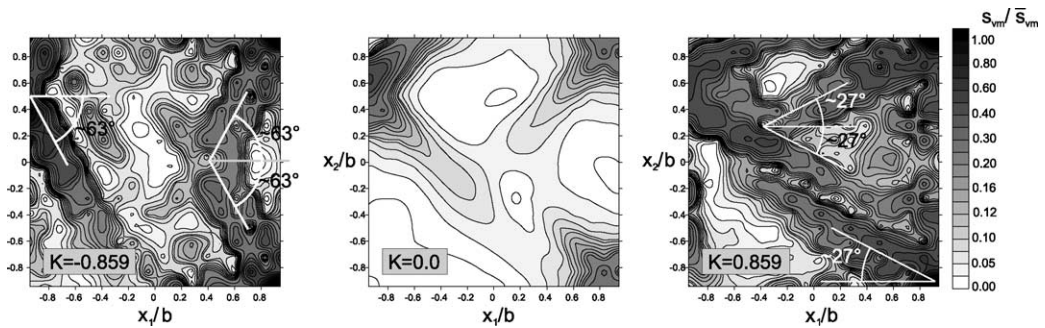


Fig. 17. Van Hove conditions: level sets of von Mises stress increment at different values of pre-stress k ($c/b = 4/9$ in Fig. 13).

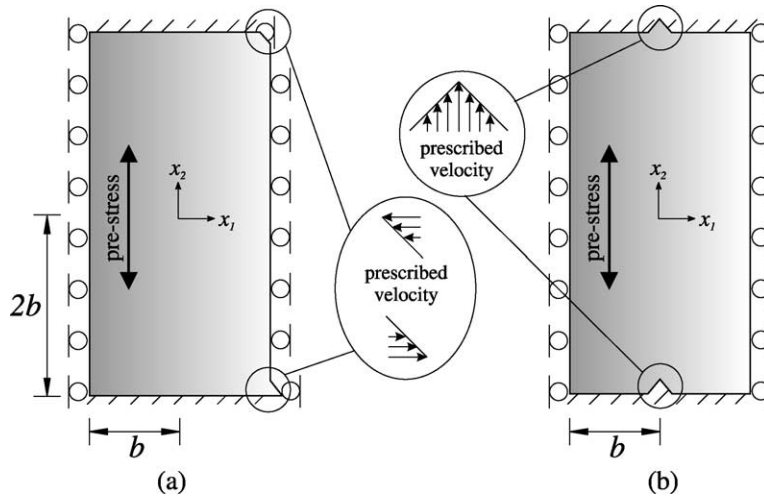


Fig. 18. Loading geometries in weak van Hove conditions.

van Hove conditions, the current situation is again defined unless an arbitrary value of homogeneous pressure. Level sets of the velocity are plotted in Figs. 19 and 21, for different values of pre-stress

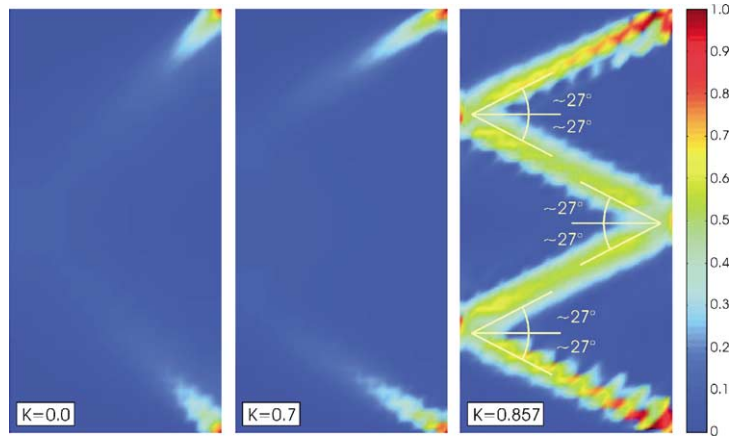


Fig. 19. Weak van Hove conditions: level sets of velocity modulus at different values of pre-stress k (Fig. 18a).

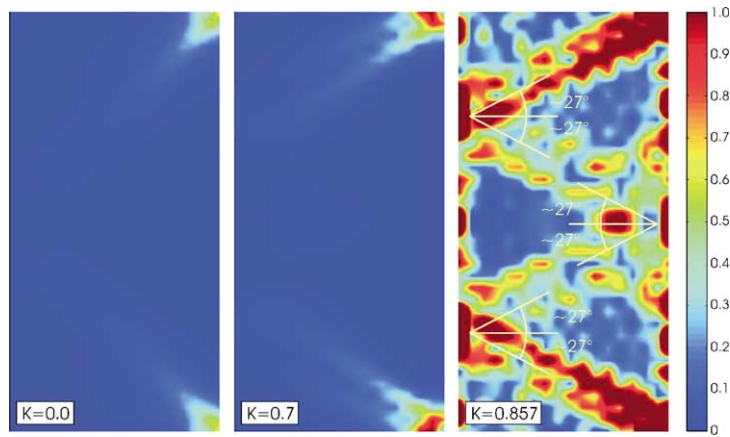


Fig. 20. Weak van Hove conditions: level sets of von Mises stress increment at different values of pre-stress k (Fig. 18a).

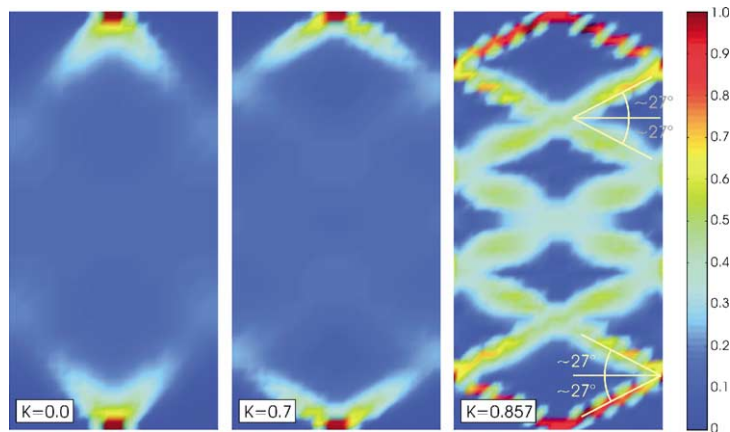


Fig. 21. Weak van Hove conditions: level sets of velocity modulus at different values of pre-stress k (Fig. 18b).

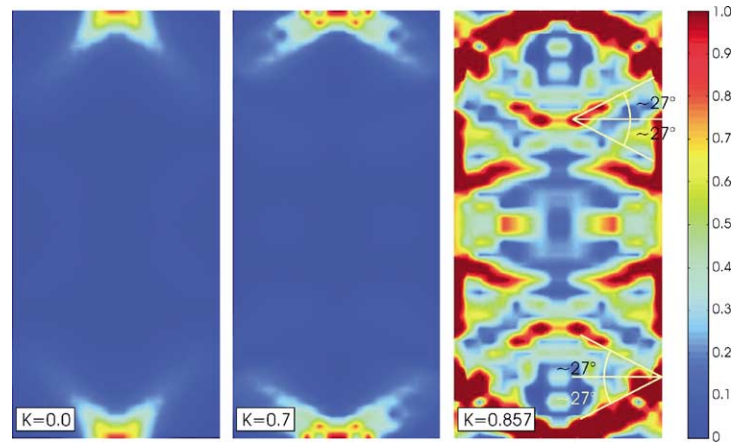


Fig. 22. Weak van Hove conditions: level sets of von Mises stress increment at different values of pre-stress k (Fig. 18b).

$k = \{0, 0.7, 0.857\}$ corresponding to compression parallel to x_2 . Level sets of the modulus of the in-plane deviatoric stress increment (8) are reported in Figs. 20 and 22. A 216-elements, uniform mesh has been employed for the boundary and 648 points for the evaluation at the internal points. Again, the Gauss points have been increased to 48 for the evaluation of integrals. We may note that until $k = 0.7$ there is no much evidence of shear banding, but this becomes evident when the boundary of loss of ellipticity is approached with $k = 0.857$.

The examples of Figs. 19–22 show that *peculiar deformation patterns emerge*, due to ‘reflection’ of shear bands at the boundary. This feature of localized deformation has been observed in different contexts (behaviour of porous plastic materials [54], dynamics of visco-plastic solids, [20,21]) and could be exploited to explain pattern formation in living tissues or in geological structures. In particular, the adaptive substructuring of trabecular bone shown in [26] (their Fig. 4) displays similarities to the pattern of Fig. 21, whereas the deformation patterns in granular media evidenced in [22] (their Fig. 4) exhibit a similarity to the pattern of Fig. 19.

The obtained patterns of deformation may also suggest a number of technological applications. For instance, we may easily speculate that the highly strained regions could transmit signals in a very localized way, so that the pre-stress may become a parameter controlling delay lines with special properties.

4. Conclusions

The boundary element technique proposed in Part I of this study has been employed to investigate bifurcation of elastic structures. Shear band formation has also been considered, for configurations pre-strained in the vicinity to the elliptic boundary. Numerical treatment of such conditions reveals the emergence of peculiar localized deformations which may explain certain mechanisms of pattern formation in nature and may suggest innovative technological applications.

Acknowledgements

Financial support of the University of Trento (D.B. and M.B.) and of the University of Ferrara (D.C.) is gratefully acknowledged.

Appendix A. Failure of ellipticity and regime classification

In a two-dimensional setting, condition (6) can be rewritten as

$$g_j n_i \mathbb{K}_{ijhk} n_h g_k = 0, \quad (\text{A.1})$$

with

$$\{\mathbf{n}\} = \{\cos \alpha, \sin \alpha\}, \quad \{\mathbf{g}\} = \{-\sin \alpha, \cos \alpha\}. \quad (\text{A.2})$$

Assuming now

$$\begin{aligned} \mathbb{K}_{1111} &= \mu_* - \frac{\sigma}{2} - p, & \mathbb{K}_{1122} &= -\mu_*, & \mathbb{K}_{1112} &= \mathbb{K}_{1121} = 0, \\ \mathbb{K}_{2211} &= -\mu_*, & \mathbb{K}_{2222} &= \mu_* + \frac{\sigma}{2} - p, & \mathbb{K}_{2212} &= \mathbb{K}_{2221} = 0, \\ \mathbb{K}_{1212} &= \mu + \frac{\sigma}{2}, & \mathbb{K}_{1221} &= \mathbb{K}_{2112} = \mu - p, & \mathbb{K}_{2121} &= \mu - \frac{\sigma}{2}, \end{aligned} \quad (\text{A.3})$$

condition (A.2) yields the two equivalent equations

$$\begin{aligned} 1 - k + (2k - 4 + 4\mu_*/\mu) \cos^2 \alpha + 4(1 - \mu_*/\mu) \cos^4 \alpha &= 0, \\ \mu \sin^4 \alpha [(1 + k) \cot^4 \alpha + 2(2\mu_*/\mu - 1) \cot^2 \alpha + 1 - k] &= 0, \end{aligned} \quad (\text{A.4})$$

the latter of which is the usual basis for the regime classification [11,25]. In particular, the absence of real solutions defines the elliptic range, while two real solutions the parabolic, and four real solutions the hyperbolic regime.

References

- [1] M.H. Aliabadi, Boundary element formulations in fracture mechanics, *Appl. Mech. Rev.* 50 (1997) 83–96.
- [2] F. Armero, On the characterization of localized solutions in inelastic solids: an analysis of wave propagation in a softening bar, *Comput. Methods Appl. Mech. Engrg.* 191 (2001) 181–213.
- [3] F. Armero, K. Garikipati, An analysis of strong discontinuities in multiplicative finite strain plasticity and their relation with the numerical simulation of strain localization in solids, *Int. J. Solids Struct.* 33 (1996) 2863–2885.
- [4] J.P. Bardet, Finite-element analysis of surface instability in hypoelastic solids, *Comput. Methods Appl. Mech. Engrg.* 78 (1990) 273–296.
- [5] Z.P. Bazant, M. Belytschko, T.P. Chang, Continuum theory for strain-softening, *ASCE J. Engrg. Mech.* 110 (1984) 1666–1691.
- [6] T. Belytschko, J. Fish, B. Englemann, A finite element with embedded localization zones, *Comput. Methods Appl. Mech. Engrg.* 70 (1988) 59–89.
- [7] A. Benallal, R. Billardon, G. Geymonat, Some mathematical aspects of the damage softening problem, in: J. Mazar, Z.P. Bazant (Eds.), *Cracking and Damage*, vol. 1, 1988, pp. 247–258.
- [8] A. Benallal, R. Billardon, G. Geymonat, Bifurcation and localization in rate-independent materials: some general considerations, in: *CISM Lecture Notes No. 327*, Springer, Berlin, 1993, pp. 1–47.
- [9] A. Benallal, C.A. Fudoli, W.S. Venturing, An implicit BEM formulation for gradient plasticity and localization phenomena, *Int. J. Numer. Methods Engrg.* 53 (2002) 1853–1869.
- [10] D. Bigoni, Bifurcation and instability of non-associative elastoplastic solids, in: H. Petryk (Ed.), *Material Instabilities in Elastic and Plastic Solids*, *CISM Lecture Notes No. 414*, Springer, Berlin, 2000, pp. 1–52.
- [11] D. Bigoni, D. Capuani, Green's function for incremental nonlinear elasticity: shear bands and boundary integral formulation, *J. Mech. Phys. Solids* 50 (2002) 471–500.
- [12] D. Bigoni, M. Gei, On bifurcation of a layered, orthotropic, elastic medium, XXVIII AIAS National Congress, Vicenza, Italy, 8–11 September 1999.
- [13] D. Bigoni, M. Ortiz, A. Needleman, Effect of interfacial compliance on bifurcation of a layer bonded to a substrate, *Int. J. Solids Struct.* 34 (1997) 4305–4326.
- [14] M.A. Biot, *Mechanics of Incremental Deformations*, John Wiley and Sons, New York, 1965.

- [15] R.I. Borja, Finite element simulation of strain localization with large deformation: capturing strong discontinuity using a Petrov–Galerkin multiscale formulation, *Comput. Methods Appl. Mech. Engrg.* 191 (2002) 2949–2978.
- [16] R. de Borst, L.J. Sluys, Localization in a Cosserat continuum under static and dynamic loading conditions, *Comput. Methods Appl. Mech. Engrg.* 90 (1991) 805–827.
- [17] B.D. Coleman, M.L. Hodgon, On shear bands in ductile materials, *Arch. Rat Mech. Anal.* 90 (1985) 219–247.
- [18] T.A. Cruse, *Boundary Element Analysis in Computational Fracture Mechanics*, Kluwer Academic Press, Dordrecht, 1988.
- [19] P. D’Ambrosio, D. De Tommasi, S. Marzano, Nonlinear elastic deformations and stability of laminated rubber bearings, *ASCE J. Engrg. Mech.* 121 (1995) 1041–1048.
- [20] A. Deb, J.H. Prevost, B. Loret, Adaptive meshing for dynamic strain localization, *Comput. Methods Appl. Mech. Engrg.* 137 (1996) 285–306.
- [21] A. Deb, B. Loret, J.H. Prevost, Automated band identification procedure for dynamic strain localization, *Comput. Methods Appl. Mech. Engrg.* 137 (1996) 307–330.
- [22] J. Desrués, R. Chambon, Shear band analysis and shear moduli calibration, *Int. J. Solids Struct.* 39 (2002) 3757–3776.
- [23] N.A. Fleck, J.W. Hutchinson, A phenomenological theory for strain gradient effects in plasticity, *J. Mech. Phys. Solids* 41 (1993) 1825–1857.
- [24] N.A. Fleck, J.W. Hutchinson, Strain gradient plasticity, in: *Advances in Applied Mechanics*, vol. 33, Academic Press, New York, 1997, pp. 295–361.
- [25] R. Hill, J.W. Hutchinson, Bifurcation phenomena in the plane tension test, *J. Mech. Phys. Solids* 23 (1975) 239–264.
- [26] R. Huiskes, R. Ruimerman, G.H. van Lenthe, J.D. Janssen, Effects of mechanical forces on maintenance and adaptation of form in trabecular bone, *Nature* 405 (2000) 704–706.
- [27] J.W. Hutchinson, V. Tvergaard, Surface instabilities on statically strained plastic solids, *Int. J. Mech. Sci.* 22 (1980) 339–354.
- [28] M. Lizuka, A macroscopic model for predicting large-deformation behaviors of laminated rubber bearings, *Engrg. Struct.* 22 (2000) 323–334.
- [29] M. Imbimbo, A. De Luca, F.E. stress analysis of rubber bearing under axial loads, *Comput. Struct.* 68 (1998) 31–39.
- [30] M. Imbimbo, J.M. Kelly, Influence of material stiffening on stability of elastomeric bearings at large displacements, *ASCE J. Engrg. Mech.* 124 (1998) 1045–1049.
- [31] J.M. Kelly, *Earthquake-resistant Design with Rubber*, Springer-Verlag, Berlin, 1997.
- [32] R. Larsson, K. Runesson, N.S. Ottosen, Discontinuous displacement approximation for capturing plastic localization, *Int. J. Numer. Methods Engrg.* 36 (1993) 2087–2105.
- [33] J.B. Leblond, G. Perrin, J. Devaux, Bifurcation effects in ductile metals with nonlocal damage, *J. Appl. Mech.* 61 (1994) 236–242.
- [34] B. Loret, J.H. Prevost, Dynamic strain localization in elasto-(visco-)plastic solids. Part 1: General formulation and one-dimensional examples, *Comput. Methods Appl. Mech. Engrg.* 83 (1990) 247–273.
- [35] H.B. Mühlhaus, I. Vardoulakis, The thickness of shear bands in granular materials, *Geotechnique* 37 (1987) 271–283.
- [36] A. Menzel, P. Steinmann, On the continuum formulation of higher gradient plasticity for single and polycrystals, *J. Mech. Phys. Solids* 48 (2000) 1777–1796.
- [37] A. Nacar, A. Needleman, M. Ortiz, A finite element method for analyzing localization in rate dependent solids at finite strains, *Comput. Methods Appl. Mech. Engrg.* 73 (1989) 235–258.
- [38] A. Needleman, Material rate dependence and mesh sensitivity in localization problems, *Comput. Methods Appl. Mech. Engrg.* 67 (1988) 69–85.
- [39] J. Oliver, On the discrete constitutive models induced by strong discontinuity kinematics and continuum constitutive equations, *Int. J. Solids Struct.* 37 (2000) 7207–7229.
- [40] H. Petryk, On energy criteria of plastic instability, in: *Plastic Instability, Proc. Considère Memorial. Ecole Nat. Fonts Chauss.*, Paris, 1985, pp. 215–226.
- [41] H. Petryk, K. Thermann, Post-critical plastic deformation of biaxially stretched sheets, *Int. J. Solids Struct.* 33 (1996) 689–705.
- [42] H. Petryk, K. Thermann, Post-critical plastic deformation in incrementally nonlinear materials, *J. Mech. Phys. Solids* 50 (2002) 925–954.
- [43] S. Pietruszczak, Z. Mróz, Finite element analysis of deformation of strain-softening materials, *Int. J. Numer. Methods Engrg.* 17 (1981) 327–334.
- [44] G. Pijaudier-Cabot, Z.P. Bazant, Nonlocal damage theory, *ASCE J. Engrg. Mech.* 113 (1987) 1512–1533.
- [45] E. Radi, D. Bigoni, D. Capuani, Effects of pre-stress on crack-tip fields in elastic, incompressible solids, *Int. J. Solids Struct.* 39 (2002) 3971–3996.
- [46] E.I. Ryzhak, On stable deformation of “unstable” materials in a rigid triaxial testing machine, *J. Mech. Phys. Solids* 41 (1993) 1345–1356.
- [47] E.I. Ryzhak, On stability of homogeneous elastic bodies under boundary-conditions weaker than displacement conditions, *Quart. J. Mech. Appl. Math.* 47 (1994) 663–672.
- [48] E.I. Ryzhak, A case of indispensable localized instability in elastic-plastic solids, *Int. J. Solids Struct.* 36 (1999) 4669–4691.

- [49] J.C. Simo, J. Oliver, F. Armero, An analysis of strong discontinuities induced by softening solutions in rate-independent solids, *J. Comput. Mech.* 12 (1993) 277–296.
- [50] L.J. Sluys, Y. Estrin, The analysis of shear banding with a dislocation based gradient plasticity model, *Int. J. Solids Struct.* 37 (2000) 7127–7142.
- [51] J.F. Stanton, G. Scroggins, A.W. Taylor, C.W. Roeder, Stability of aminated elastomeric bearings, *ASCE J. Engrg. Mech.* 116 (1990) 1351–1371.
- [52] N. Triantafyllidis, E. Aifantis, A gradient approach to localization of deformation: I. Hyperelastic materials, *J. Elast.* 16 (1986) 225–237.
- [53] H.-C. Tsai, S.-J. Hsueh, Mechanical properties of isolation bearings identified by a viscoelastic model, *Int. J. Solids Struct.* 38 (2001) 53–74.
- [54] V. Tvergaard, Influence of void nucleation on ductile shear fracture at a free surface, *J. Mech. Phys. Solids* 30 (1982) 399–425.
- [55] L. van Hove, Sur l'extension de la condition de Legendre du calcul des variations aux intégrales multiples à plusieurs fonctions inconnues, *Proc. Sect. Sci. K. Akad. van Wetenschappen, Amsterdam*, vol. 50, 1947, pp. 18–23.
- [56] I. Vardoulakis, E. Aifantis, A gradient flow theory of plasticity for granular materials, *Acta Mech.* 87 (1991) 197–217.
- [57] N.B.J. Young, Bifurcation phenomena in the plane compression test, *J. Mech. Phys. Solids* 24 (1976) 77–91.